Environ. Sci.: Nano, 2021,8, 122-130

Journal Name

ARTICLE

Beneficial Synergy of Adsorption-Intercalation-Conversion Mechanisms in Nb_2O_5@Nitrogen-Doped Carbon Frameworks for Promoted Removal of Metal Ions via Hybrid Capacitive Deionization

Received 00th January 20xx,
Accepted 00th January 20xx

DOI: 10.1039/x0xx00000x

www.rsc.org/

Guizhi Wang[†], Tingting Yan[†], Junjie Shen[‡], Jianping Zhang[†], Liyi Shi[†], and Dengsong Zhang*[†]

Capacitive deionization (CDI) is an emerging water purification technology, but the ion adsorption capacity of traditional carbon-based CDI electrodes is still unsatisfactory. Herein, a novel faradaic electrode by anchoring Nb_2O_5 nanoparticles on the nitrogen-doped carbon frameworks as anodes and activated carbon (AC) as cathodes in a hybrid capacitive deionization (HCDI) system was originally developed to capture Na^+ ions via the adsorption-intercalation-conversion mechanisms. The synergetic effects of nanostructure and carbon coating were beneficial to enhancing electrical conductivity and offering fast Na^+ ions diffusion pathways. Impressively, the HCDI system demonstrated an excellent ion adsorption capacity of 35.4 mg g^{-1} in a 500 mg L^{-1} NaCl solution at 1.2 V as well as stable regeneration ability. In situ Raman and ex situ XPS measurements unraveled that the mechanism of ions removal from water was the reversible redox reaction of Nb_2O_5. The new overall understanding of synergetic effects opens opportunities for the design of HCDI systems for efficient removal of metal ions from saline water.

1 Introduction

In recent decades, the shortage of clean water has become a global issue as a consequence of population growth and climate change.[1-3] Less than 3% of all water on earth is fresh water, and only 1.2% of all fresh water is surface water which can be directly utilized. With this limited amount usable fresh water, desalination of saline water and brackish water offers a promising solution to the supply of clean water.[4, 5] Traditional desalination methods have been examined to remove ions from seawater efficiently. Unfortunately, some of the methods suffer from various drawbacks including massive energy consumption, high cost and significant environmental impact.[6, 7] Therefore, it is imperative to develop cost-effective and eco-friendly desalination technologies as promising alternatives. Capacitive deionization (CDI) has gained increasing attention due to its unique advantages of low energy consumption, low cost, rapid regeneration, and environmentally harmlessness.[8, 9] When applying a low potential on the two electrodes, the ions in solution can be quickly adsorbed and harvested in the oppositely-charged electrodes. Thus, the clean water is obtained.[10, 11]

The ion removal capacity of CDI is closely dependent on the electrode materials. Carbon-based materials, such as carbon aerogels, carbon nanotubes, activated carbon, mesoporous carbon, and reduced graphene, have been extensively explored as CDI electrode materials due to the advantages of high surface area, porous structure, and electrochemical stability.[12-15] Unfortunately, one of the major limitations of carbon-based materials is the unsatisfactory ion adsorption capacity.[16, 17] In carbon-based electrodes, the ions removed from solution are reserved on the carbon surface based on the electric double layer (EDL) theory, in which the removal capacity is mainly determined by the pores and surface area. In addition, the co-ions effect would restrain more ions from gathering and cause absorbed ions to easily return to the solution.[18, 19] To overcome the drawback, hybrid capacitive deionization (HCDI) has been developed. HCDI systems consist of one carbon electrode and one faradaic electrode.[20, 21] In general, anions (such as Cl^- ions) are electrostatic adsorbed on the carbon-based materials. But cations (such as Na^+ ions) are not only removed by surface adsorption, but also captured through a charge transfer reaction.[22, 23] Compared with those EDL-based electrodes, HCDI systems deliver higher ion removal capacity and faster ion removal rates.[24, 25] The selection of faradic materials for HCDI systems usually favored those with substantially improved energy storage domains.[26, 27] Back in

[†] *State Key Laboratory of Advanced Special Steel, School of Materials Science and Engineering, International Joint Laboratory of Catalytic Chemistry, Research Center of Nano Science and Technology, Department of Chemistry, College of Sciences, Shanghai University, No.99 Shangda Road, Shanghai, 200444, China.*
[‡] *Department of Chemical Engineering, University of Bath, Bath BA2 7AY, UK.*
[*] *E-mail: dszhang@shu.edu.cn; Tel: +86 21 66137152.*

Electronic supplementary information (ESI) available: materials, structural characterization, electrochemical characterization, CDI test, SEM images, TEM images, Particle size distribution, SAED pattern, EDS, XRD pattern, N_2 adsorption-desorption isotherms, BJH pore size distribution plots, XPS spectra, Dynamic water contact angle analysis, CV curves, Specific capacitance, GCD curves, IR drop, plots of IAC vs. deionization time, Ragone plots, Comparison between AIAR and CR, Regeneration test, Elemental quantification, Fitted parameters in EIS, and comparison of IAC with other reported materials. See DOI: 10.1039/x0xx00000x

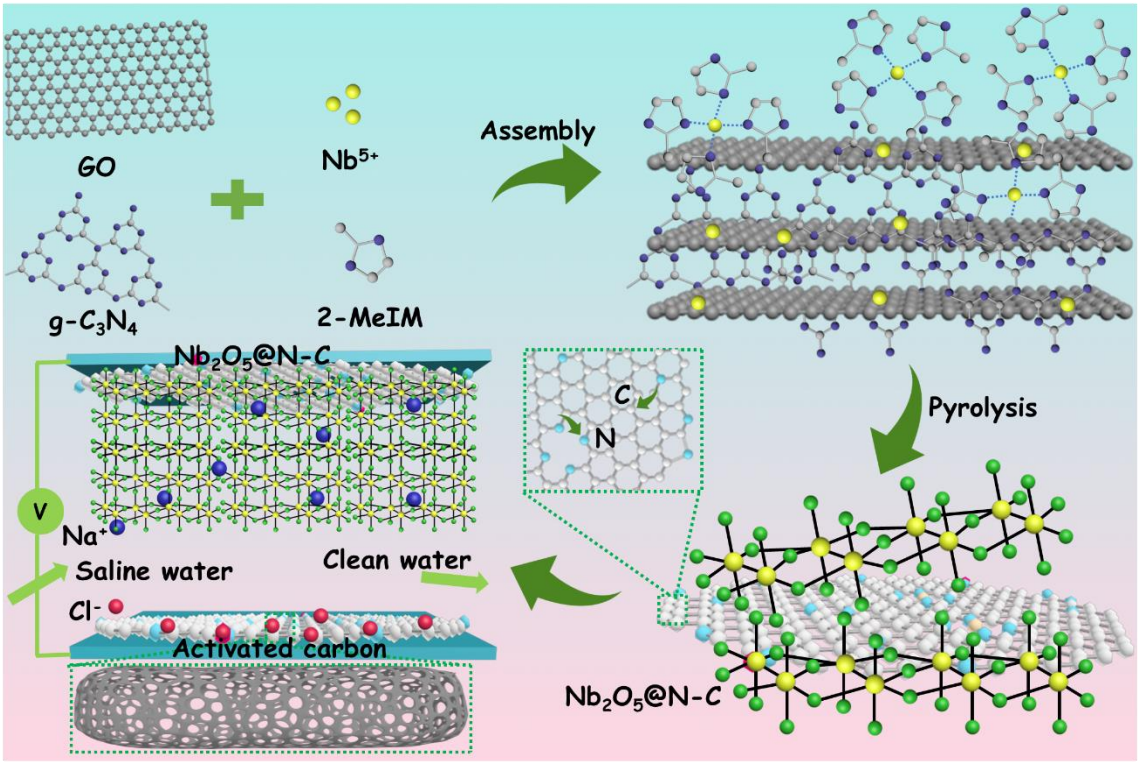

Figure 1. Schematic illustration of Nb_2O_5@N-C composites as anodes for hybrid capacitive deionization.

2012, Pasta[28] et al. selected $Na_{2-x}Mn_5O_{10}$ and Ag as the electrodes and obtained good desalination performance. After that, a series of faradic electrode materials, such as MnO_2, TiO_2, SnS_2, MoS_2, $Na_4Ti_9O_{20}$, $NaTi_2(PO_4)_3$, and Prussian blue, have been developed and proved to gain excellent ion removal capacities.[29-32] Wang[33] et al. used the hollow carbon@MnO_2 to capture Na^+ ions through redox reaction and obtained a high removal capacity of 30.7 mg g^{-1}. Our former work[34] synthesized MoS_2–graphene materials to reserve/convert Na^+ ions via faradaic reaction. The obtained electrodes demonstrated a high volumetric adsorption capacity of 14.3 mg cm^{-3} in a 500 mg L^{-1} NaCl solution at 1.2 V.

Orthorhombic Nb_2O_5 (T-Nb_2O_5), as a representative Na^+ ions capture material with intercalation-conversion type, is a promising candidate HCDI electrode due to the intrinsic structural advantage.[35, 36] The (001) planes of Nb_2O_5 has a larger interplanar spacing (3.9 Å) than the size of Na^+ ions (2.04 Å), which may be suitable for Na^+ ions diffusion.[37] Unfortunately, the low electrical conductivity (≈3 × 10^{-6} S cm^{-1}) and the sluggish diffusion of Na^+ ions from aggregation tendency may hinder the further application of Nb_2O_5. Two effective methods can be adopted to enhance the electrical conductivity and decrease the diffusion length for electrons/ions: (1) nanostructure engineering can turn the materials into low dimensions, which offers shorter pathways and faster Na^+ ions diffusion;[38, 39] (2) composite with carbon can stabilize the materials and form an interconnected network for fast transport of electron and Na^+ ions.[40, 41] Throughout all sorts of carbon-based supports, graphene gains much attention due to large surface area, good chemical/physical stability, and superb electrical conductivity.[42] Moreover, the heteroatoms (such as nitrogen) doped in the carbon skeleton could boost electrical conductivity, introduce more defects, and improve hydrophilicity.[43, 44] Graphitic carbon nitride (g-C_3N_4), as a suitable nitrogen precursor, has a relatively high nitrogen content of 57% and sp^2 hybridized carbon structure. The high level of pyridine type nitrogen can offer abundant lone electron pairs to capture Nb atoms as benign ligands.[45] 2-Methylimidazole, as another benign N ligand, can coordinate with Nb and prohibit the large aggregation of Nb_2O_5 nanocrystals during the heating process at elevated temperature.[46]

Herein, we originally designed Nb_2O_5 anchored on nitrogen-doped carbon frameworks (denoted as Nb_2O_5@N-C-1) via simple assembly and pyrolysis as anodes and activated carbon (AC) as cathodes. The obtained Nb_2O_5@N-C-1 had uniform Nb_2O_5 nanoparticles tightly anchored on the graphene networks. The N-doping improved the electrical conductivity and produced localized highly-reactive regions. Benefitting from the synergetic effects of structure optimization (nanostructure) and surface engineering (nitrogen-doped carbon coating), the Nb_2O_5@N-C-1 electrode demonstrated superior CDI performance in terms of ion adsorption capacity and ion adsorption rates. Furthermore, in situ Raman and ex situ XPS analysis were conducted to verify the adsorption-intercalation-conversion mechanism of ion removal from water during the CDI process.

2 Materials and methods

First of all, graphene oxide (GO) was prepared by a modified Hummer's method,[39] and g-C_3N_4 was obtained by a thermal decomposition/polymerization process.[46] Specifically, 0.02 g of GO and 0.1 g of g-C_3N_4 were mixed in 50 mL of methanol after ultrasonic treatment for 1 h. Next, 0.11 g of $NbCl_5$ was added into the mixture after ultrasonic treatment for 0.5 h to form solution Alpha. Meanwhile, 0.17 g of 2-Methylimidazole (2-MeIM) was dispersed in 30 mL of methanol after ultrasonic treatment for 0.5 h to form solution Beta. Then, solution Beta was dropwise added into solution Alpha with stirring, and the mixed solution was left at room temperature for 12 h. The Nb/2MeIM/g-C_3N_4/GO precursors were gained by centrifugation with methanol and drying at 60 °C for 12 h. After that, the dried material was calcined at 800 °C (3 °C/min) for 2 h under an N_2 condition to obtain Nb_2O_5@N-C-1 ($NbCl_5$ and 2-MeIM with mole ratio of 1:1) composite. Simultaneously, Nb_2O_5@N-C-2 (0.11 g of $NbCl_5$ and 0.085 g of 2-MeIM with mole ratio of 2:1), Nb_2O_5@N-C-0.5 (0.11 g of $NbCl_5$ and 0.34 g of 2-MeIM with mole ratio of 1:2), Nb_2O_5 (only utilization of $NbCl_5$) and N-C (without utilization of $NbCl_5$) were synthesized through similar procedure.

3 Results and discussion

3.1 Characteristics Analysis

These Nb_2O_5@N-C composites were synthesized via an assembly approach followed by a pyrolysis method at 800 °C under a N_2 condition, as shown in Figure 1. In the assembly process, Nb^{5+} ions were readily adsorbed on the surface of the negative charged GO/g-C_3N_4 complex and further coordinated with 2-Methylimidazole (2-MeIM) to form the Nb/2MeIM/g-C_3N_4/GO precursors (Figure S1a, b). After the pyrolysis treatment, the Nb_2O_5@N-C composites were successfully prepared. The morphology and microstructure of the obtained samples were observed and verified by SEM and TEM (Figure S2). These electron microscopes images revealed that Nb_2O_5 nanoparticles with an average size of around 50 nm (Figure S2c, S2f, and S2i) were tightly anchored on the nitrogen-doped graphene sheets. Besides, the density of Nb_2O_5 nanocrystals increased with the improvement of Nb^{5+} utilization, from Nb_2O_5@N-C-0.5 (Figure S2a, b), Nb_2O_5@N-C-1 (Figure S2d, e) to Nb_2O_5@N-C-2 (Figure S2g, h). The contact between Nb_2O_5 nanoparticles and graphene network (Figure 2a) could supply numerous pathways for ion diffusion and electron transfer, which would improve the electrochemical performance. The HRTEM image of Nb_2O_5@N-C-1 ((Figure 2b) displayed lattice fringes with a spacing of 0.393 nm, which were well attached to the (001) planes of the orthorhombic Nb_2O_5 phase. In Figure S3, prominent diffraction rings were observed in the selected area electron diffraction (SAED) patterns, which confirmed the existence of (001), (180), and (200) planes of the orthorhombic Nb_2O_5 phase. Furthermore, the relevant elemental mapping images of Nb_2O_5@N-C-1 demonstrated uniform distributions of C, N, O, and Nb elements over the selected area, which proved that the Nb_2O_5 nanoparticles were homogeneously anchored on the nitrogen-doped graphene networks (Figure S4).

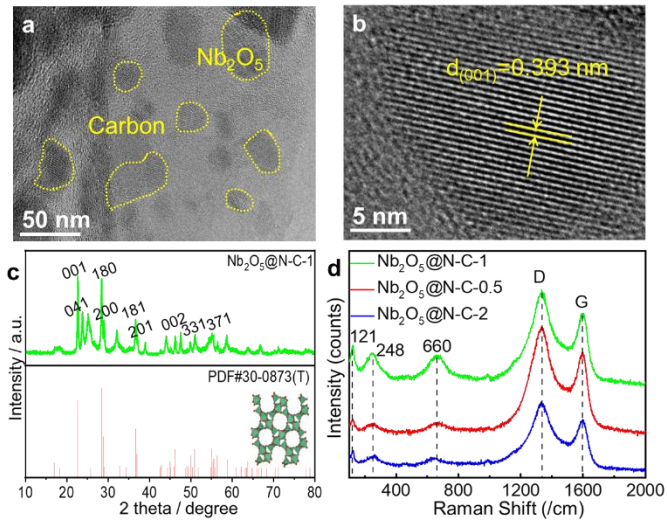

Figure 2. (a) TEM image, (b) HRTEM image, (c) XRD pattern of Nb_2O_5@N-C-1, and (d) Raman spectra of Nb_2O_5@N-C-0.5, Nb_2O_5@N-C-1, and Nb_2O_5@N-C-2.

The formation and crystalline structure of the Nb_2O_5 nanocrystals in these Nb_2O_5@N-C composites were verified by the XRD analysis, as shown in Figure 2c and Figure S5. These characteristic diffraction peaks located at 22.6°, 25.7°, 28.4°, 28.9°, 36.6°, 37.0°, 46.2°, 50.9°, and 54.9°, could be appropriately indexed to (001), (041), (180), (200), (181), (201), (002), (331), and (371) planes of the orthorhombic Nb_2O_5 phase (PDF#30-0873). To figure out the composition and structural properties of the correlative carbon supports, Raman analysis of the obtained samples was conducted (Figure 2d). Two typical carbon-based characteristic peaks of disordered carbon (D band) and sp^2 bonded ordered graphitic carbon (G band) were observed at around 1350 and 1599 cm^{-1}. The value of I_D/I_G was normally related to the degree of structural disorder and the number of defects. The I_D/I_G values of Nb_2O_5@N-C-0.5, Nb_2O_5@N-C-1, and Nb_2O_5@N-C-2 were 1.19, 1.16, and 1.11, revealing the abundant vacancies and defects. Moreover, the degree of disorder decreased with the increase of metal contents. Besides, the three small peaks at 121, 248, and 660 cm^{-1} were the characteristic bands of Nb_2O_5, which corresponded to the vibrations of octahedrons, the bending vibration of Nb-O bond, and the stretching vibration of Nb-O bond,[47, 48] respectively. The pore structure characteristics of Nb_2O_5@N-C composites were obtained by N_2 adsorption/desorption measurements. Both the BET specific surface area and pore volume decreased as the amount of Nb_2O_5 in the composite increased (Table S1). Nb_2O_5@N-C-0.5 gained the largest BET specific surface area of 78.6 m^2 g^{-1}, in comparison of Nb_2O_5@N-C-1 of 34.1 m^2 g^{-1} and Nb_2O_5@N-C-2 of 29.5 m^2 g^{-1} (Figure S6a). Moreover, the pore size distribution plots indicated the mesoporous structures of the three samples, which could supply abundant diffusion channels for ions transportation. Specifically, Nb_2O_5@N-C-1 showed a similar pore size and volume distribution compared to Nb_2O_5@N-C-0.5, much higher and richer than Nb_2O_5@N-C-2 in the range of 2-10 nm (Figure S6b). To further investigate the surface chemical elements and bonding states of the Nb_2O_5@N-C composites, XPS analysis was conducted, as shown in Figure S7. The Nb 3d, C 1s, N 1s, and O 1s signals

were obviously seen in the full-scan spectra of Nb_2O_5@N-C-0.5, Nb_2O_5@N-C-1, and Nb_2O_5@N-C-2, proving the successful integration of Nb_2O_5 in the structure of carbon frameworks. Moreover, the formation of C-N bond (Figure S8) confirmed the insertion of N atoms into the carbon plane. The N 1s peak consisted of four types of N, namely pyridinic N, pyrrolic N, graphitic N, and oxide N (Figure S9). The Nb-O bond (Figure S10) verified the presence of Nb_2O_5. The atomic percentage of Nb element (Table S2) increased from Nb_2O_5@N-C-0.5 to Nb_2O_5@N-C-2, which was consistent with the Nb precursors utilization in the synthesis process. Since the electrochemical properties and CDI performance were tested in NaCl aqueous solution, the hydrophilicity of the electrode materials was also a vital indicator. We evaluated the hydrophilicity by dynamic water contact angle test (Figure S11). The results showed that Nb_2O_5@N-C-1 had a smaller contact angle (74.29°) than Nb_2O_5@N-C-0.5 (75.42°) and Nb_2O_5@N-C-2 (84.14°). The good hydrophilicity of Nb_2O_5@N-C-1 was due to the porous structure and abundant N content within the carbon frameworks.

3.2 Electrochemical Performance

The electrochemical performance of Nb_2O_5@N-C composites was firstly evaluated by cyclic voltammetry (CV). The CV plots were obtained at scan rates ranging from 1 to 100 mV s^{-1} (Figure S12a-c). For every composite, the integrated area of CV curve was gradually enlarged with the increase of scan rates. At the same scan rate, the Nb_2O_5@N-C-1 curve had the largest integrated area, followed by the Nb_2O_5@N-C-0.5 and Nb_2O_5@N-C-2 curves. As a result, the Nb_2O_5@N-C-1 possessed the highest specific capacitance among these composites at any scan rate (Figure S12d). To gain a deeper insight into the charge transfer mechanisms in Nb_2O_5@N-C-1, we quantitatively divided the contributions of capacitive and diffusion-controlled effects from CV plots by using a slower scan rate of 0.1 mV s^{-1}. In Figure 3a, a redox peak appeared at around -0.13 V, demonstrating a faradic reaction of Na^+ ions inserting into the Nb_2O_5@N-C-1 electrode. Therefore, the Na^+ ions are removed by the synergetic effects of electro-adsorption of the nitrogen-doped carbon frameworks and faradaic reaction of Nb_2O_5 (Figure S13). The surface capacitive (shade areas) and diffusion-controlled contributions of Nb_2O_5@N-C-1 at 0.1 mV s^{-1} were 64.3% and 35.7%, respectively.[37, 49] The results confirmed that Nb_2O_5 played a leading role in capturing Na^+ ions. Figure S14a-c indicated the galvanostatic charge-discharge (GCD) plots of Nb_2O_5@N-C-0.5, Nb_2O_5@N-C-1, and Nb_2O_5@N-C-2 at a current density of 0.2, 0.4, 0.6, 0.8, 1.0 and 1.2 A g^{-1}. The GCD plots demonstrated analogous symmetric triangular shapes, exhibiting benign electrochemical reversibility. Besides, when the current density was raised from 0.2 to 1.2 A g^{-1}, the Nb_2O_5@N-C-1 electrode showed the longest discharge time, which manifested the largest capacitance in accordance with the CV results. Additionally, Nb_2O_5@N-C-1 showed a lower potential drop (iR) than other materials at the initial discharge process (Figure S14d), suggesting a better electrical resistance. Cycling stability was another vital parameter for electrode materials. In Figure 3b, the GCD plots maintained the original shape after 10000 cycles at 10 A g^{-1}, manifesting an outstanding cycle-to-cycle durability. The superior electrochemical property of Nb_2O_5@N-C-1 was further demonstrated by electrochemical impedance spectroscopy (EIS), as shown in Figure 3c. The Nyquist plots consisted of a semicircle in the medium frequency region corresponding to charge-transfer resistance (R_{ct}), and a straight segment in the low frequency region corresponding to Warburg diffusion impedance (W). An equivalent circuit (inset of Figure 3c) was employed to simulate these EIS curves, in which R_s and CPE_{ct} represented solution resistance and constant phase part, respectively.[50] Nb_2O_5@N-C-1 demonstrated the smallest semicircle among the three electrodes, indicating the lowest charge-transfer impedance. According to the fitting results (Table S3), the R_{ct} values were 14.66, 18.52, and 23.94 Ω for Nb_2O_5@N-C-1, Nb_2O_5@N-C-0.5, and Nb_2O_5@N-C-2, respectively. Furthermore, the diffusion coefficient (D_{Na^+}) of Nb_2O_5@N-C-1 was 4.18×10^{-15} cm^2 s^{-1}, much larger than those of Nb_2O_5@N-C-0.5 (2.49×10^{-15} cm^2 s^{-1}) and Nb_2O_5@N-C-2 (2.27×10^{-15} cm^2 s^{-1}), indicating an enhanced Na^+ ions diffusion and adsorption (Figure 3d). Therefore, the excellent electrochemical properties may endow Nb_2O_5@N-C-1 with good CDI performance.

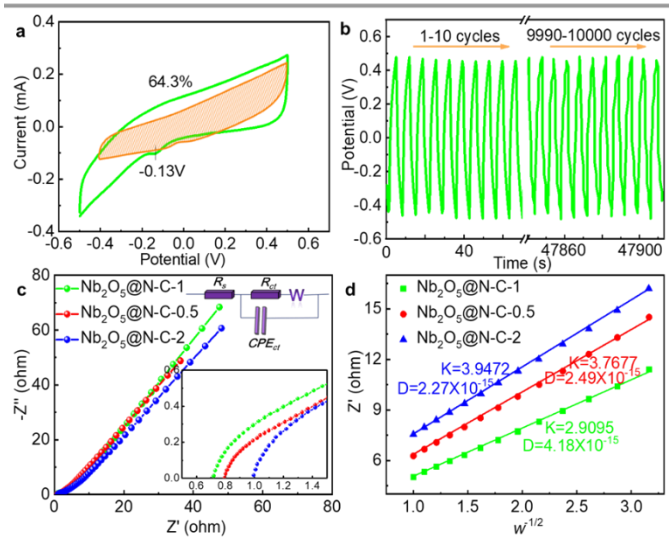

Figure 3. (a) Total current (green line) and capacitive current (shade regions) of Nb_2O_5@N-C-1 at 0.1 mV s^{-1}, (b) 10000 GCD curves of Nb_2O_5@N-C-1 in the first 10 cycles and the last 10 cycles at 10 A g^{-1}, (c) EIS of Nb_2O_5@N-C-0.5, Nb_2O_5@N-C-1, and Nb_2O_5@N-C-2, inset: the equivalent circuit to simulate EIS curves, and (d) The corresponding plots of real part impedance (Z') vs. squared root of the angular frequency ($\varpi^{-1/2}$) in the Warburg region.

3.3 Capacitive Deionization of Water

The batch-mode CDI experiments were conducted to evaluate the removal capacity of the electrode pairs. In Figure 4a, the deionization behaviors of Nb_2O_5//AC, Nb_2O_5@N-C-0.5//AC, Nb_2O_5@N-C-1//AC and Nb_2O_5@N-C-2//AC were analyzed in a 500 mg L^{-1} NaCl solution at 1.2 V. It was observed that the ion adsorption capacity (IAC) increased quickly at first and then the trend is gradually slowdown within the required time. The Na^+ ions were removed through electro-adsorption

and electrochemical reactions with Nb_2O_5@N-C, while the negatively charged Cl^- ions were electrically-adsorbed by the AC electrode. After 120 min, the IAC of Nb_2O_5@N-C-1//AC reached 35.4 mg g^{-1}, much higher than those of Nb_2O_5@N-C-0.5//AC, Nb_2O_5@N-C-2//AC, and Nb_2O_5//AC which were 29.2 mg g^{-1}, 19.4 mg g^{-1}, and 10.4 mg g^{-1}, respectively. The result confirmed that the combinations of Nb_2O_5 composite with nitrogen-doped carbon framework can enhance the removal capacity of pure metal oxides. In addition to IAC, the ion adsorption rate (IAR) is another key indicator of the CDI performance. Figure 4b showed the Ragone plots of IAR vs. IAC of the four electrodes. IAR was located at a high level firstly and moved downwards with the increase of IAC. The Ragone plot of Nb_2O_5@N-C-1//AC was located at the top right corner, suggesting that Nb_2O_5@N-C-1//AC had the fastest ion adsorption rate as well as the highest removal capacity among the four electrode materials. Additionally, to demonstrate the advantages of Nb_2O_5@N-C-1//AC over simple carbon substrate and the advantages of nitrogen-doped carbon framework over commercial AC, the desalination behavior of Nb_2O_5@N-C-1//AC along with N-C//AC and AC//AC were tested in a 500 mg L^{-1} NaCl solution at 1.2 V. Unsurprisingly, the Nb_2O_5@N-C-1//AC composites exhibited the largest IAC and the quickest IAR (Figure S15). The outstanding performance of Nb_2O_5@N-C-1//AC was further confirmed in Figure S16 where Nb_2O_5@N-C-1//AC exhibited the greatest concentration reduction (CR) (0.88 mM) and the fastest average ion adsorption rate (AIAR) (0.50 mg g^{-1} min^{-1}) among all the electrode materials. The charge utilization and energy loss in the CDI process could be measured by charge efficiency. The charge efficiencies of Nb_2O_5@N-C-0.5//AC, Nb_2O_5@N-C-1//AC, Nb_2O_5@N-C-2//AC, and Nb_2O_5//AC were calculated using the current transient curves in a 500 mg L^{-1} NaCl solution at 1.2 V. As shown in Figure 4c, Nb_2O_5@N-C-1//AC had a higher charge efficiency (0.70) than Nb_2O_5@N-C-0.5//AC (0.58), Nb_2O_5@N-C-2//AC (0.46) and Nb_2O_5//AC (0.31). A series of trade-off curves between the inverse of specific energy consumption (SEC^{-1}) and IAR were also recorded in a 500 mg L^{-1} NaCl solution at 1.2 V. In Figure 4d, the trade-off curve of Nb_2O_5@N-C-1//AC was always above the curves of Nb_2O_5@N-C-0.5//AC, Nb_2O_5@N-C-2//AC, and Nb_2O_5//AC. This means Nb_2O_5@N-C-1//AC reached the fastest IAR in the same SEC^{-1} compared with other electrodes, demonstrating the most efficient energy utilization. The synergetic effects of electro-adsorption of nitrogen-doped carbon framework and faradaic reaction of Nb_2O_5 facilitated ion diffusion and ions adsorption. The deionization property of Nb_2O_5@N-C-1//AC was further analyzed at various initial concentrations of NaCl solution and different applied voltages. In Figure 4e, it was clear that the IAC of Nb_2O_5@N-C-1//AC increased from 18.1, 27.4, to 35.4 mg g^{-1} as the NaCl concentrations increased from 100, 300, to 500 mg L^{-1} at 1.2 V. In general, a higher NaCl concentration reduced the ionic resistance and facilitated fast ion adsorption. Compared with other reported metal-based electrode materials (Table S4), Nb_2O_5@N-C-1 exhibited excellent deionization behavior with high ion adsorption capacity. Moreover, the Ragone plot moved to the top right with the increase of NaCl concentration, verifying a faster IAR and a higher IAC in a 500 mg L^{-1} solution (Figure S17a). Figure 4f presented the IAC of Nb_2O_5@N-C-1//AC at distinct applied voltages of 0.8, 1.0, and 1.2 V. The change of voltages was consistent with the change of NaCl concentrations. Notably, IAC increased from 4.9, 19.1, to 35.4 mg g^{-1} when the voltage was raised from 0.8, 1.0, to 1.2 V. The Ragone plots (Figure S17b) also showed a faster IAR and a higher IAC at a higher voltage. The enhanced deionization performance was due to the stronger electrostatic force at a higher applied voltage. The comparison between CR and AIAR in different combinations of NaCl concentration and voltage also showed that the best performance was achieved when the initial NaCl concentration was 500 mg L^{-1} and the applied voltage was 1.2 V (Figure S18). The regeneration ability was crucial to justifying a deionization material for further applications. The continuous cyclic adsorption-desorption experiments of Nb_2O_5@N-C-1//AC were conducted in a 100 mg L^{-1} NaCl solution (Figure S19). The adsorption process was started by applying a 1.2 V voltage, and the subsequent desorption process was realized by short circuiting at 0 V. In every cycle, the electrical conductivity dropped to a low level during the adsorption process and recovered to the initial level

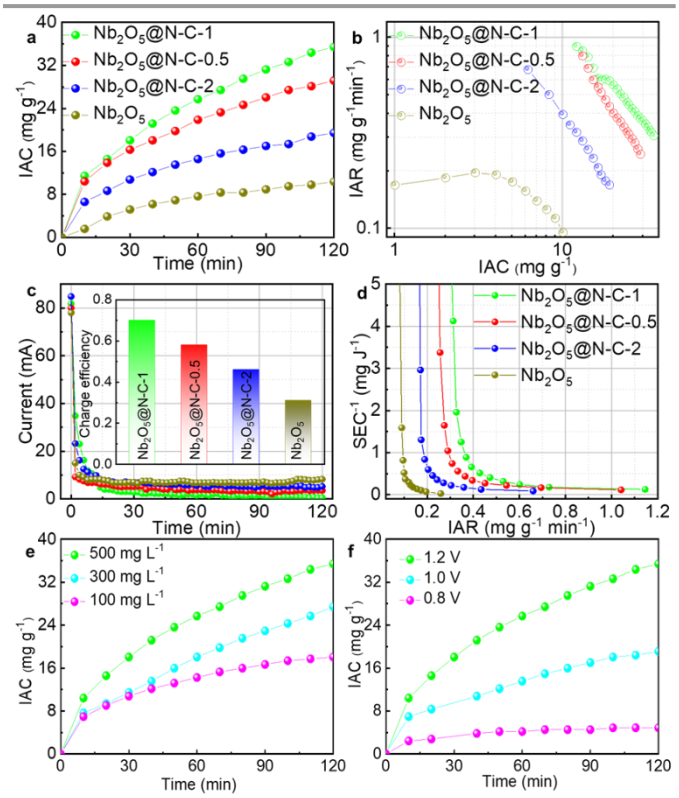

Figure 4. (a) IAC plots of Nb_2O_5, Nb_2O_5@N-C-0.5, Nb_2O_5@N-C-1, and Nb_2O_5@N-C-2 electrodes in a 500 mg L^{-1} NaCl solution with a working voltage of 1.2 V and flow rate of 40 mL min^{-1}, (b) The corresponding Ragone plots of IAR vs. IAC of the three electrodes, (c) Current transient curves and charge efficiency (insert figure) of Nb_2O_5, Nb_2O_5@N-C-0.5, Nb_2O_5@N-C-1, and Nb_2O_5@N-C-2 electrodes in a 500 mg L^{-1} NaCl solution with a working voltage of 1.2 V and flow rate of 40 mL min^{-1}, (d) Plots of the trade-off between SEC^{-1} and SAR of Nb_2O_5, Nb_2O_5@N-C-0.5, Nb_2O_5@N-C-1, and Nb_2O_5@N-C-2 electrode materials, (e) IAC plots of Nb_2O_5@N-C-1 in a different initial concentration of NaCl solution with a working voltage of 1.2 V and flow rate of 40 mL min^{-1}, (f) IAC plots of Nb_2O_5@N-C-1 in a 500 mg L^{-1} NaCl solution with different working voltage and flow rate of 40 mL min^{-1}.

during the desorption process. The water recovery (WR) was 33.3%, the energy consumption was 100 J g^{-1} and energy efficiency was 19.58% under same measurement condition in one cycle. The deionization rate demonstrated general stability over 20 consecutive adsorption-desorption cycles. After the regeneration test, the Nb_2O_5 nanoparticles were still tightly anchored on the nitrogen-doped graphene sheets (Figure S20a, b). But the size of Nb_2O_5 nanoparticles slightly decreased, which could shorten ion transport pathways and provide rapid diffusion channels in a long-term operation (Figure S20c). The above results proved that Nb_2O_5@N-C-1 possessed outstanding regeneration ability.

3.4 Mechanisms of Ions Removal

The mechanisms of ions removal from water were investigated by in situ Raman characterization. Figure 5a recorded the in-situ Raman spectra when the CV plots (scan rate of 0.1 mV s^{-1}) reached to different stages of ion adsorption and desorption (Figure S21). During the ion adsorption process from 0.5 to -0.5 V, the evolution of each band could be summarized as follows. (1) the V_{Hi} band kept nearly constant from 0.5 to 0.1 V. When the potential decreased to -0.1 V, the V_{Hi} band demonstrated a red shift and the relative intensity increased, which was consistent with the CV curves in which a prominent cathodic peak appeared at this range. (2) the V_{Mid} band presented a similar trend with the V_{Hi} band. No noticeable change was observed from 0.5 to 0.1 V. After that, the V_{Mid} band split into two small bands from -0.1 to -0.5 V. (3) the V_{Lo} band, after being static at the range from 0.5 to 0.1 V, demonstrated an increased relative intensity from -0.1 V. In contrast, the evolution of the three bands in Na^+ ions deintercalation process was the exact opposite of the above-mentioned Na^+ ions intercalation. Specifically, during the ion desorption process from -0.5 to 0.5 V, the V_{Hi} band was blue-shifted with a reduced intensity; the V_{Mid} bands merged into one band; and the V_{Lo} band also decreased in intensity. The opposite evolutions of these Raman band groups of Nb_2O_5 verified the reversible structural conversion via Na^+ ions intercalation/deintercalation.[51, 52] Moreover, ex situ XPS analysis was used to observe the valence changes in Nb element during the ion adsorption and ion desorption process. As shown in Figure S22, there was a clear blue shift from the pristine state to the adsorption state and the subsequent red shift from the adsorption state to the desorption state. The reversible shift of Nb $3d_{5/2}$ and Nb $3d_{3/2}$ revealed that the valence changes of Nb had a strong correlation with the Na^+ ions conversion process. The Nb 3d XPS spectra of the three states were divided into individual peaks to provide more information about the removal mechanisms (Figure 5b). At the pristine state, Nb^{5+} played a significant role while Nb^{4+} was in the minority. After that, the majority of Nb^{5+} were reduced into Nb^{4+} when the electrode adsorbed sufficient Na^+ ions. Finally, most Nb^{4+} were oxidized to Nb^{5+} after the applied voltage was removed. The above XPS results indicated that the Na^+ ions conversion process arose from the reversible redox reaction of the Nb^{5+}/Nb^{4+} pair in the Nb_2O_5@N-C-1 electrode.[53-55] The Na^+ ions insertion/extraction reaction could be expressed as $Nb_2O_5 + x\ Na^+ + x\ e^- \Leftrightarrow Na_xNb_2O_5$.[38, 53] Meanwhile, Cl^- ions were adsorbed on the surface of the positively charged AC during the ion adsorption process, and released back to the salt solution during the ion desorption process. Therefore, the removal mechanisms of Na^+ ion and Cl^- ion could be distinctly illustrated in Figure 5c.

4 Conclusions

In summary, the exceptional CDI performance of Nb_2O_5@N-C-1 could be explained by the synergetic effects of electro-adsorption of nitrogen-doped carbon framework and faradaic reaction of Nb_2O_5. GO, g-C_3N_4 and 2-MeIM derived nitrogen-doped carbon (N-C) as the flexible support showed superb

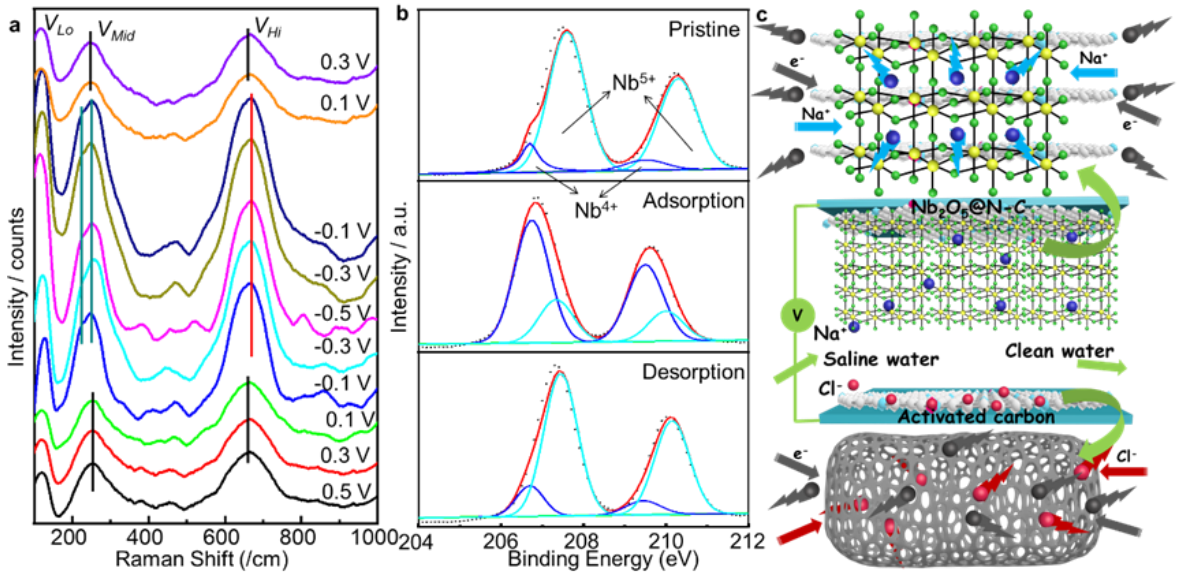

Figure 5. (a) In-situ Raman tests of Na^+ ions adsorption/desorption behavior in Nb_2O_5@N-C-1, (b) The corresponding valence change of Nb during the pristine, adsorption, and desorption process, and (c) Schematic illustration of ions removal mechanisms in Nb_2O_5@N-C-1.

cycling stability. Besides, the introduction of N-C enhanced the electrical conductivity of Nb_2O_5 and realized a better Na^+ ions diffusion. Nb_2O_5 in-situ growth on the N-C framework increased the ion diffusion channels and facilitated the fast transport of Na^+ ion. Owing to the combination of electro-adsorption/desorption mechanism of N-C and insertion/extraction process of Nb_2O_5, the Nb_2O_5@N-C-1 electrode displayed an excellent ion removal capacity. Inspiringly, the novel HCDI system equipped with Nb_2O_5@N-C-1//AC exhibited superb IAC (35.4 mg g^{-1} in a 500 mg L^{-1} NaCl solution at 1.2 V), fast IAR, high charge efficiency, low energy loss, and good regeneration ability. In situ Raman and ex situ XPS analysis verified that the mechanisms of ions removal were reversible intercalation and faradaic reaction of Nb_2O_5. This work presents a new strategy to design highly efficient HCDI systems for water purification.

Conflicts of interest

There are no conflicts to declare.

Acknowledgements

The authors acknowledge the support of the National Natural Science Foundation of China (21906101; 21722704) and the Science and Technology Commission of Shanghai Municipality (19DZ2293100; 18DZ2281400).

Notes and references

1. T. Oki and S. Kanae, Global Hydrological Cycles and World Water Resources, Science, 2006, 313, 1068.
2. C. J. Vörösmarty, P. B. McIntyre, M. O. Gessner, D. Dudgeon, A. Prusevich, P. Green, S. Glidden, S. E. Bunn, C. A. Sullivan, C. R. Liermann and P. M. Davies, Global threats to human water security and river biodiversity, Nature, 2010, 467, 555-561.
3. G. Wang, T. Yan, J. Zhang, L. Shi and D. Zhang, Trace-Fe-Enhanced Capacitive Deionization of Saline Water by Boosting Electron Transfer of Electro-Adsorption Sites, Environ. Sci. Technol., 2020, 54, 8411-8419.
4. J.-F. Pekel, A. Cottam, N. Gorelick and A. S. Belward, High-resolution mapping of global surface water and its long-term changes, Nature, 2016, 540, 418-422.
5. M. Elimelech and W. A. Phillip, The Future of Seawater Desalination: Energy, Technology, and the Environment, Science, 2011, 333, 712.
6. J. E. Dykstra, R. Zhao, P. M. Biesheuvel and A. van der Wal, Resistance identification and rational process design in Capacitive Deionization, Water Res., 2016, 88, 358-370.
7. C. Zhang, D. He, J. Ma, W. Tang and T. D. Waite, Faradaic reactions in capacitive deionization (CDI)-problems and possibilities: A review, Water Res., 2018, 128, 314-330.
8. S. P. Surwade, S. N. Smirnov, I. V. Vlassiouk, R. R. Unocic, G. M. Veith, S. Dai and S. M. Mahurin, Water desalination using nanoporous single-layer graphene, Nature Nanotechnol., 2015, 10, 459-464.
9. C. He, J. Ma, C. Zhang, J. Song and T. D. Waite, Short-Circuited Closed-Cycle Operation of Flow-Electrode CDI for Brackish Water Softening, Environ. Sci. Technol., 2018, 52, 9350-9360.
10. P. Liu, T. Yan, L. Shi, H. S. Park, X. Chen, Z. Zhao and D. Zhang, Graphene-based materials for capacitive deionization, J. Mater. Chem. A, 2017, 5, 13907-13943.
11. T. Wang, C. Zhang, L. Bai, B. Xie, Z. Gan, J. Xing, G. Li and H. Liang, Scaling behavior of iron in capacitive deionization (CDI) system, Water Res., 2020, 171, 115370.
12. J. Zhang, T. Yan, J. Fang, J. Shen, L. Shi and D. Zhang, Enhanced capacitive deionization of saline water using N-doped rod-like porous carbon derived from dual-ligand metal-organic frameworks, Environ. Sci.: Nano, 2020, 7, 926-937.
13. Z. U. Khan, T. Yan, J. Han, L. Shi and D. Zhang, Capacitive deionization of saline water using graphene nanosphere decorated N-doped layered mesoporous carbon frameworks, Environ. Sci.: Nano, 2019, 6, 3442-3453.
14. W. Tang, J. Liang, D. He, J. Gong, L. Tang, Z. Liu, D. Wang and G. Zeng, Various cell architectures of capacitive deionization: Recent advances and future trends, Water Res., 2019, 150, 225-251.
15. F. Ji, L. Wang, J. Yang, X. Wu, M. Li, S. Jiang, S. Lin and Z. Chen, Highly compact, free-standing porous electrodes from polymer-derived nanoporous carbons for efficient electrochemical capacitive deionization, J. Mater. Chem. A, 2019, 7, 1768-1778.
16. Y.-W. Chen, J.-F. Chen, C.-H. Lin and C.-H. Hou, Integrating a supercapacitor with capacitive deionization for direct energy recovery from the desalination of brackish water, Appl. Energy, 2019, 252, 113417.
17. F. Yu, L. Wang, Y. Wang, X. Shen, Y. Cheng and J. Ma, Faradaic reactions in capacitive deionization for desalination and ion separation, J. Mater. Chem. A, 2019, 7, 15999-16027.
18. J. Cao, Y. Wang, L. Wang, F. Yu and J. Ma, $Na_3V_2(PO_4)_3$@C as Faradaic Electrodes in Capacitive Deionization for High-Performance Desalination, Nano Lett., 2019, 19, 823-828.
19. L. Wang, J. E. Dykstra and S. Lin, Energy Efficiency of Capacitive Deionization, Environ. Sci. Technol., 2019, 53, 3366-3378.
20. M. Li and H. G. Park, Pseudocapacitive Coating for Effective Capacitive Deionization, ACS Appl. Mater. Interfaces, 2018, 10, 2442-2450.
21. F. Zhou, T. Gao, M. Luo and H. Li, Heterostructured graphene@$Na_4Ti_9O_{20}$ nanotubes for asymmetrical capacitive deionization with ultrahigh desalination capacity, Chem. Eng. J., 2018, 343, 8-15.
22. F. Xing, T. Li, J. Li, H. Zhu, N. Wang and X. Cao, Chemically exfoliated MoS_2 for capacitive deionization of saline water, Nano Energy, 2017, 31, 590-595.
23. Y. Zhao, B. Liang, X. Wei, K. Li, C. Lv and Y. Zhao, A core-shell heterostructured CuFe@NiFe Prussian blue analogue as a novel electrode material for high-capacity and stable capacitive deionization, J. Mater. Chem. A, 2019, 7, 10464-10474.
24. K. Wang, Y. Liu, Z. Ding, Y. Li, T. Lu and L. Pan, Metal-organic-frameworks-derived $NaTi_2(PO_4)_3$/carbon composites for efficient hybrid capacitive deionization, J. Mater. Chem. A, 2019, 7, 12126-12133.
25. Z. Yue, T. Gao and H. Li, Robust synthesis of carbon@$Na_4Ti_9O_{20}$ core-shell nanotubes for hybrid capacitive deionization with enhanced performance, Desalination, 2019, 449, 69-77.
26. B. W. Byles, D. A. Cullen, K. L. More and E. Pomerantseva, Tunnel structured manganese oxide nanowires as redox active electrodes for hybrid capacitive deionization, Nano Energy, 2018, 44, 476-488.
27. W. Peng, W. Wang, G. Han, Y. Huang and Y. Zhang, Fabrication of 3D flower-like MoS_2/graphene composite as high-performance electrode for capacitive deionization, Desalination, 2020, 473, 114191.

28. M. Pasta, C. D. Wessells, Y. Cui and F. La Mantia, A Desalination Battery, Nano Lett., 2012, 12, 839-843.
29. Z. Y. Leong and H. Y. Yang, A Study of MnO_2 with Different Crystalline Forms for Pseudocapacitive Desalination, ACS Appl. Mater. Interfaces, 2019, 11, 13176-13184.
30. X. Wen, M. Zhao, M. Zhang, X. Fan and D. Zhang, Efficient Capacitive Deionization of Saline Water by an Integrated Tin disulfide Nanosheet@Graphite Paper Electrode via an in Situ Growth Strategy, ACS Sustain. Chem. Eng., 2019, 8, 1268-1275.
31. M. Ding, S. Fan, S. Huang, M. E. Pam, L. Guo, Y. Shi and H. Y. Yang, Tunable Pseudocapacitive Behavior in Metal-Organic-Framework-Derived TiO_2@Porous Carbon Enabling High-Performance Membrane Capacitive Deionization, ACS Appl. Energy Mater., 2019, 2, 1812-1822.
32. B. H. Min, J.-H. Choi and K. Y. Jung, Improved capacitive deionization of sulfonated carbon/titania hybrid electrode, Electrochim. Acta, 2018, 270, 543-551.
33. S. Wang, G. Wang, T. Wu, C. Li, Y. Wang, X. Pan, F. Zhan, Y. Zhang, S. Wang and J. Qiu, Membrane-Free Hybrid Capacitive Deionization System Based on Redox Reaction for High-Efficiency NaCl Removal, Environ. Sci. Technol., 2019, 53, 6292-6301.
34. J. Han, T. Yan, J. Shen, L. Shi, J. Zhang and D. Zhang, Capacitive Deionization of Saline Water by Using MoS_2–Graphene Hybrid Electrodes with High Volumetric Adsorption Capacity, Environ. Sci. Technol., 2019, 53, 12668-12676.
35. B. Deng, T. Lei, W. Zhu, L. Xiao and J. Liu, In-Plane Assembled Orthorhombic Nb_2O_5 Nanorod Films with High-Rate Li^+ Intercalation for High-Performance Flexible Li-Ion Capacitors, Adv. Funct. Mater., 2018, 28, 1704330.
36. P. Guo, K. Sun, X. Shang, D. Liu, Y. Wang, Q. Liu, Y. Fu and D. He, Nb_2O_5/RGO Nanocomposite Modified Separators with Robust Polysulfide Traps and Catalytic Centers for Boosting Performance of Lithium-Sulfur Batteries, Small, 2019, 15, e1902363.
37. X. Wang, Q. Li, L. Zhang, Z. Hu, L. Yu, T. Jiang, C. Lu, C. Yan, J. Sun and Z. Liu, Caging Nb_2O_5 Nanowires in PECVD-Derived Graphene Capsules toward Bendable Sodium-Ion Hybrid Supercapacitors, Adv. Mater., 2018, 30, e1800963.
38. D. Cao, Z. Yao, J. Liu, J. Zhang and C. Li, H-Nb_2O_5 wired by tetragonal tungsten bronze related domains as high-rate anode for Li-ion batteries, Energy Storage Mater., 2018, 11, 152-160.
39. G.-Z. Wang, J.-M. Feng, L. Dong, X.-F. Li and D.-J. Li, Antimony (IV) Oxide Nanorods/Reduced Graphene Oxide as the Anode Material of Sodium-ion Batteries with Excellent Electrochemical Performance, Electrochim. Acta, 2017, 240, 203-214.
40. K. Tang, T. Z. X. Hong, L. You and K. Zhou, Carbon-metal compound composite electrodes for capacitive deionization: synthesis, development and applications, J. Mater. Chem. A, 2019, 7, 26693-26743.
41. B. W. Byles, B. Hayes-Oberst and E. Pomerantseva, Ion Removal Performance, Structural/Compositional Dynamics, and Electrochemical Stability of Layered Manganese Oxide Electrodes in Hybrid Capacitive Deionization, ACS Appl. Mater. Interfaces, 2018, 10, 32313-32322.
42. J. Han, L. Shi, T. Yan, J. Zhang and D. Zhang, Removal of ions from saline water using N, P co-doped 3D hierarchical carbon architectures via capacitive deionization, Environ. Sci.: Nano, 2018, 5, 2337-2345.
43. J. Zhang, J. Fang, J. Han, T. Yan, L. Shi and D. Zhang, N, P, S co-doped hollow carbon polyhedra derived from MOF-based core-shell nanocomposites for capacitive deionization, J. Mater. Chem. A, 2018, 6, 15245-15252.
44. P. Liu, H. Wang, T. Yan, J. Zhang, L. Shi and D. Zhang, Grafting sulfonic and amine functional groups on 3D graphene for improved capacitive deionization, J. Mater. Chem. A, 2016, 4, 5303-5313.
45. R. Wang, T. Yan, L. Han, G. Chen, H. Li, J. Zhang, L. Shi and D. Zhang, Tuning the dimensions and structures of nitrogen-doped carbon nanomaterials derived from sacrificial g-C_3N_4/metal-organic frameworks for enhanced electrocatalytic oxygen reduction, J. Mater. Chem. A, 2018, 6, 5752-5761.
46. G. Wang, J. Deng, T. Yan, J. Zhang, L. Shi and D. Zhang, Turning on electrocatalytic oxygen reduction by creating robust Fe-N_x species in hollow carbon frameworks via in situ growth of Fe doped ZIFs on g-C_3N_4, Nanoscale, 2020, 12, 5601-5611.
47. Q. Deng, F. Chen, S. Liu, A. Bayaguud, Y. Feng, Z. Zhang, Y. Fu, Y. Yu and C. Zhu, Advantageous Functional Integration of Adsorption-Intercalation-Conversion Hybrid Mechanisms in 3D Flexible Nb_2O_5@Hard Carbon@MoS_2@Soft Carbon Fiber Paper Anodes for Ultrafast and Super-Stable Sodium Storage, Adv. Funct. Mater., 2020, 30, 1908665.
48. X. Jiao, Q. Hao, X. Xia, Z. Wu and W. Lei, Metal organic framework derived Nb_2O_5@C nanoparticles grown on reduced graphene oxide for high-energy lithium ion capacitors, Chem. Commun., 2019, 55, 2692-2695.
49. H. Kim, E. Lim, C. Jo, G. Yoon, J. Hwang, S. Jeong, J. Lee and K. Kang, Ordered-mesoporous Nb_2O_5/carbon composite as a sodium insertion material, Nano Energy, 2015, 16, 62-70.
50. Q. Ji, X. Gao, Q. Zhang, L. Jin, D. Wang, Y. Xia, S. Yin, S. Xia, N. Hohn, X. Zuo, X. Wang, S. Xie, Z. Xu, L. Ma, L. Chen, G. Z. Chen, J. Zhu, B. Hu, P. Müller‐Buschbaum, P. G. Bruce and Y. J. Cheng, Dental Resin Monomer Enables Unique NbO_2/Carbon Lithium-Ion Battery Negative Electrode with Exceptional Performance, Adv. Funct. Mater., 2019, 29, 1904961.
51. D. Chen, J. H. Wang, T. F. Chou, B. Zhao, M. A. El-Sayed and M. Liu, Unraveling the Nature of Anomalously Fast Energy Storage in T-Nb_2O_5, J. Am. Chem. Soc., 2017, 139, 7071-7081.
52. J. Meng, Q. He, L. Xu, X. Zhang, F. Liu, X. Wang, Q. Li, X. Xu, G. Zhang, C. Niu, Z. Xiao, Z. Liu, Z. Zhu, Y. Zhao and L. Mai, Identification of Phase Control of Carbon-Confined Nb_2O_5 Nanoparticles toward High-Performance Lithium Storage, Adv. Energy Mater., 2019, 9, 1802695.
53. Y. Li, H. Wang, L. Wang, Z. Mao, R. Wang, B. He, Y. Gong and X. Hu, Mesopore-Induced Ultrafast Na^+-Storage in T-Nb_2O_5/Carbon Nanofiber Films toward Flexible High-Power Na-Ion Capacitors, Small, 2019, 15, e1804539.
54. F. Liu, X. Cheng, R. Xu, Y. Wu, Y. Jiang and Y. Yu, Binding Sulfur-Doped Nb_2O_5 Hollow Nanospheres on Sulfur-Doped Graphene Networks for Highly Reversible Sodium Storage, Adv. Funct. Mater., 2018, 28, 1800394.
55. Y. Lian, D. Wang, S. Hou, C. Ban, J. Zhao and H. Zhang, Construction of T-Nb_2O_5 nanoparticles on/in N-doped carbon hollow tubes for Li-ion hybrid supercapacitors, Electrochim. Acta, 2020, 330, 135204.

